

Unicorn: U-Net for Sea Ice Forecasting with Convolutional Neural Ordinary Differential Equations

Jaesung Park^{1,†}, Sungchul Hong^{2,†}, Yoonseo Cho¹, and Jong-June Jeon^{1,2,*}

¹:Department of Statistical Data Science, University of Seoul

²:Department of Statistics, University of Seoul

[†]: Co-first authors

*: corresponding author, jj.jeon@uos.ac.kr

Abstract

Sea ice at the North Pole is vital to global climate dynamics. However, accurately forecasting sea ice poses a significant challenge due to the intricate interaction among multiple variables. Leveraging the capability to integrate multiple inputs and powerful performances seamlessly, many studies have turned to neural networks for sea ice forecasting. This paper introduces a novel deep architecture named Unicorn, designed to forecast weekly a spatial configuration of sea ice. Our model integrates temporal sequences of images within its architecture to enhance its forecasting performance. Moreover, we incorporate a bottleneck layer within the U-Net architecture, serving as neural ordinary differential equations with convolutional operations, to capture the spatiotemporal dynamics of latent variables. Through real data analysis, our proposed model demonstrates significant improvements over state-of-the-art models in the sea ice forecasting tasks. These experimental results show the superiority of our proposed model.

Keywords: sea ice forecasting, spatiotemporal forecasting, deep learning, U-Net, neural ordinary differential equations

Many studies have highlighted the close relationship between global climate change and the Arctic over the years, particularly emphasizing the role of sea ice Notz and Stroeve (2016). The phenomenon of Arctic amplification, where temperatures in the Arctic are rising at a rate four times higher than the global average, underscores the Arctic’s position as an indicator of climate change Wunderling et al. (2020); Rantanen et al. (2022). The diminishing of sea ice has led to increased surface temperatures and lower albedo, a proportion

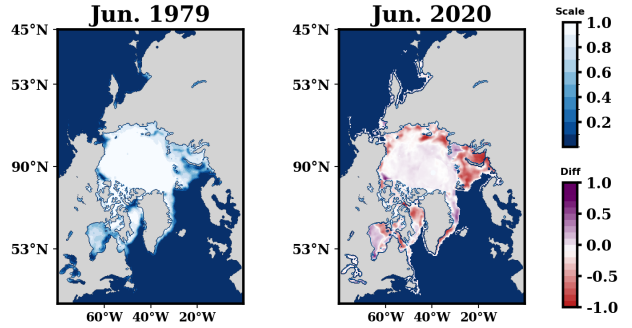


Figure 1: Monthly average sea ice concentration in June 1979 (left) and June 2020 (right). The colored regions highlight the difference in sea ice concentration between the two years.

of radiation reflected by sea ice, setting off a chain of positive climate feedback mechanisms that further fuel Arctic amplification Screen and Simmonds (2010); Pitman and Mauritsen (2014). As shown in Figure 1, there is a clear decrease in June sea ice concentration between 1979 and 2020. With ongoing anthropogenic influence, this trend is expected to continue, indicating both a shrinking of the Arctic sea ice Kwok (2018); Sumata et al. (2023). Therefore, predicting sea ice loss is crucial as it affects the local Arctic ecosystem and weather conditions in the Northern Hemisphere Li et al. (2009); Kraemer et al. (2024).

Sea ice prediction involves two primary forecasts: sea ice concentration (SIC) at the pixel level and overall sea ice extent (SIE). In predicting sea ice accurately, it’s crucial to capture the detailed dynamic changes in geographical morphology while retaining both spatial and temporal contexts. Temporally, through the time series of average SIC, we can effectively identify over-

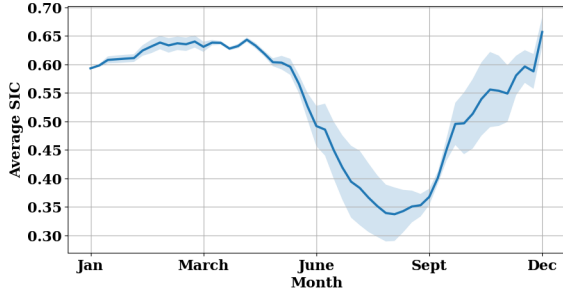


Figure 2: Trend of the averaged SIC spanning from 1998 to 2021. The blue band indicates the average ± 1 standard deviation.

all patterns of SIC. The average SIC time series from January to December, as shown in Figure 2, highlights a prominent trend, with its lowest point in August and peak sea ice concentration in December. Spatially, the patterns can be identified by visualizing the sea ice edge. As illustrated in Figure 3, the sea ice edge in July undergoes inward during a decreasing trend or in October outward shifts during an increasing trend, while the interior remains relatively stable. It’s worth noting that the sea ice forecaster models both temporal and spatial dynamics simultaneously.

Sea ice forecasting has relied on physical and statistical models designed to capture the inherent complexity of the phenomenon Wang et al. (2013); Collopy et al. (2015); Yuan et al. (2016). With recent advancements in deep learning, neural networks have emerged as a powerful tool capable of making predictions based on the inherent characteristics of the data Choi et al. (2019); He et al. (2022); Kim et al. (2023). IceNet Andersson et al. (2021) is a notable example of this approach, successfully using deep learning to predict sea ice edges. Additionally, Ren et al. (2022) proposes integrating various spatial attention modules with deep learning models specifically for sea ice forecasting. However, these methods still have limitations in effectively addressing non-stationarity or trend shifts and in compartmentalizing the modeling of spatial and temporal dynamics like an architecture with spatial attention followed by temporal attention.

We suggest a framework of models aiming to overcome the limitations of existing sea ice prediction models in spatiotemporal modeling through three approaches. Firstly, we introduce neural ordinary differential equations (NODE) Chen et al. (2018) and ConvNODE Paoletti et al. (2019); Li et al. (2021) to more efficient parameterization for the non-stationarity inherent in image time series. Our model extends the structure of ConvNODE to a neural network frame-

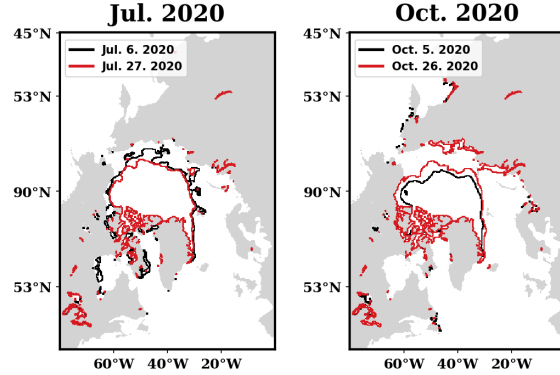


Figure 3: Sea ice edge shifts over time in July (left) and October 2020 (right).

work for spatiotemporal forecasting. Secondly, to mitigate information loss during the processing of time series components by the proposed model’s encoder, we incorporate time series component decomposition into the data input layer. Prediction models utilizing the decomposition have enhanced performance by effectively extracting trends while retaining temporal information in predictions, particularly in non-stationary time series Salles et al. (2019). Finally, our model incorporates SIC images and ancillary data, similar to IceNet’s use of climatic variables as supplementary data, further improving forecasting performance.

Building upon our new framework, this study proposes a novel SIC forecasting model named Unicorn (U-Net for sea Ice forecasting using Convolutional Operation Node). By integrating the ConvNODE into the bottleneck of the U-Net structure, Unicorn utilizes the local spatial context within the images, all while preserving the temporal order of the data input. In addition to its distinctive model architecture, we enhance performance by incorporating ancillary image data pertaining to sea ice concentration. The main contributions of our work are as follows:

- We propose an efficient deep learning architecture for fusing SIC image time series and ancillary static images to enhance forecasting accuracy.
- We introduce a novel spatiotemporal latent modeling approach utilizing neural differential equations with convolutional operations.
- In real data analysis, our proposed model outperforms the state-of-art models, including domain-specific ones, in SIC and SIE forecasting from 1 to 4 weeks ahead.

1 Related Work

This section presents various approaches to forecasting SIC, encompassing physical, statistical, and deep learning models. Wang et al. (2013); Collow et al. (2015) employed the Climate Forecast System, version 2 (CFSv2), which integrates atmospheric and oceanic dynamics alongside an interactive sea ice component, to forecast SIE. Nevertheless, these models relying on physics law entail significant computational expenses and often exhibit lower performance compared to statistical-based models. Statistical models, serving as an alternative to physical-based models, such as vector autoregression (VAR) Wang et al. (2016) and linear Markov model Yuan et al. (2016), are utilized for forecasting SIC. However, statistical models have limitations regarding forecasting over mid or long terms due to their reliance on simplistic modeling approaches and the challenge of incorporating exogenous features.

Deep learning-based approaches for sea ice forecasting have been proposed to address these limitations. In initial studies, simple neural network architectures such as multilayer perceptron (MLP), recurrent neural networks (RNN), and CNN have been employed Chi and Kim (2017); Song et al. (2018). However, these models encounter challenges in effectively capturing concurrent spatial and temporal features. To address the need for spatiotemporal representation learning and achieve higher accuracy, Convolutional LSTM (ConvLSTM) Shi et al. (2015) and U-Net Ronneberger et al. (2015) architectures have been employed.

ConvLSTM integrates Long Short-Term Memory (LSTM) and CNN layers to facilitate spatiotemporal learning Huang et al. (2023). In the context of daily SIC forecasting, ConvLSTM-based models have demonstrated superior performance compared to CNN-based models Kim et al. (2019); Liu et al. (2021). Furthermore, Kim et al. (2021) proposes the multi-task ConvLSTM to forecast both SIC and SIE simultaneously. This multi-task model exhibits superior performance by leveraging the relationships between the two tasks.

U-Net is initially designed as an encoder-decoder architecture for semantic segmentation for biomedical images. The encoder component maps inputs to lower-dimensional feature vectors by aggregating locally and globally spatiotemporal features. Subsequently, in the decoding step, these vectors are mapped back into the original feature space by exploiting the intermediate outputs of the encoder. Due to its superior performances in pixel-wise classification, U-Net has been applied to various domains beyond biomedical imaging, including weather forecasting Seo et al. (2022); Fer-

nández and Mehrkanoon (2021), and traffic forecasting Choi (2020). In SIC forecasting, Andersson et al. (2021) proposes an ensemble architecture of U-Nets, IceNet, surpassing physics-based models’ performance while maintaining computational efficiency. Additionally, Ren et al. (2022) proposed SICNet, a U-Net-based model designed for the weekly prediction of daily SIC, featuring various modules that enhance the capacity to capture spatiotemporal dependencies.

2 Dataset

This study uses observational sea-ice data from June 22, 1998, to June 14, 2021. Weekly average SIC data mapped to a (25km \times 25km) grid were provided by the Korea Polar Research Institute (KOPRI). In contrast, ancillary sea-ice age (SIA) and brightness temperature (TB) data were obtained through the National Snow and Ice Data Center (NSIDC) Tschudi et al. (2019); Meier et al. (2022). As SIC estimations can vary depending on the algorithm used for inference, we selected TB dataset as ancillary data to improve prediction and SIA to utilize the characteristics of ice age Chen et al. (2023).

The SIC data have a spatial resolution of 304 \times 448, and they are gridded to a spatial reference system EPSG code of 3411, consisting of 5 image channels, including weekly SIC, North Pole, coastline, land mask, and missing data information. The weekly SIC, North Pole, and missing data information channels are combined into one channel, while the coastline and land mask channels are used to mask out continental regions. As our primary focus is predicting SIC, we preprocess the spatial and temporal resolution of TB and SIA datasets to match our SIC dataset. For the TB dataset, we extract TB at a 37 GHz frequency channel and interpolate missing pixels using the nearest neighbor method. The daily temporal resolution of TB dataset is averaged to match the weekly temporal resolution of the SIC dataset. In the SIA dataset, we also preprocess the pixel values so that sea ice aged two years or more is grouped as multi-year sea ice, distinguishing it from first-year sea ice. As the SIA dataset has a spatial resolution of 722 \times 722 and is mapped to a (12.5km \times 12.5km) grid with a spatial reference system EPSG code of 3408, reprojection is used to standardize spatial resolution. Figure 4 visually presents all datasets and the entire data manipulation process preceding the forecasting model’s training phase.

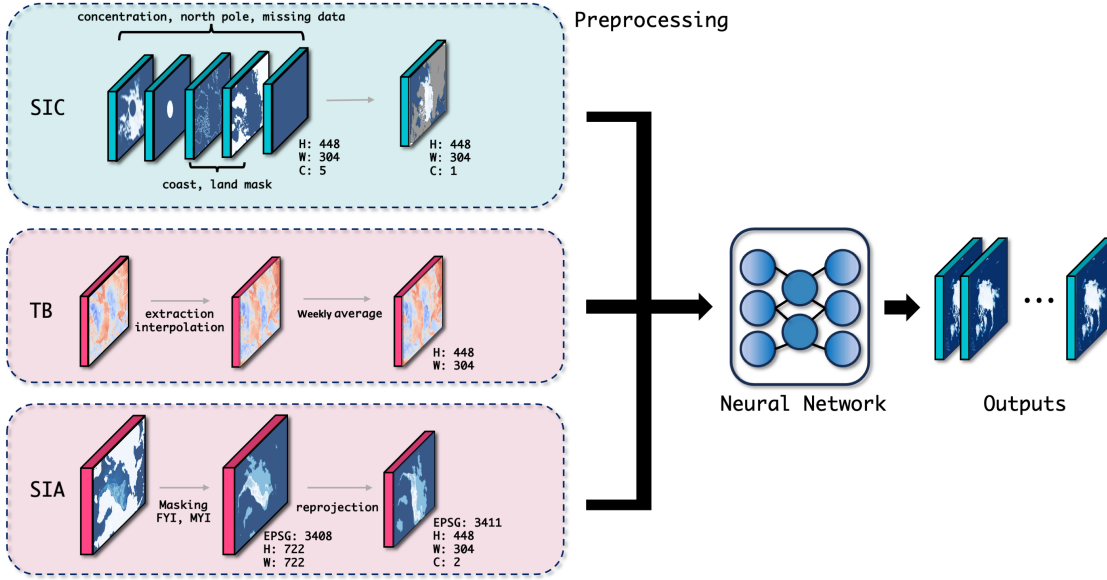


Figure 4: Preprocessing of our main SIC dataset and ancillary TB, SIA datasets acquired from KOPRI and NSIDC.

3 Proposed method

This section introduces the proposed method, Unicorn, which employs the U-Net architecture and convolutional operations as the rate of change function of latent variables. The network architecture of Unicorn is displayed in Figure 5. Unicorn consists of two U-NetNODEs, each comprising three components: the encoder, ConvNODE, and decoder. Each component is detailed in the subsequent sections. Our proposed model aims to forecast the sea ice concentration as a time series of length τ , measured in weeks. The model takes SIC image from time $(t - L + 1)$ to t , denoted as $\mathbf{X}_t \in \mathbb{R}^{L \times (H \times W)}$. Note that L represents the sequence length with consideration of the channel dimension. The dimensions H and W refer to the height and width of each image, respectively. Additionally, U-NetNODE takes ancillary datasets as inputs, the TB and SIA, as denoted $\mathbf{B}_t \in \mathbb{R}^{1 \times (H \times W)}$ and $\mathbf{S}_t \in \mathbb{R}^{2 \times (H \times W)}$, respectively. Because we consider each group of SIA described in Section 2 as a binary variable, \mathbf{S}_t has two channels. The model output consists of sea ice concentration predictions from $(t + 1)$ to $(t + \tau)$ time points, denoted as $\hat{\mathbf{Y}}_t \in [0, 1]^{\tau \times (H \times W)}$, while the corresponding target SIC is denoted as $\mathbf{Y}_t \in [0, 1]^{\tau \times (H \times W)}$. For our experiment, we set L and τ to 12 and 4, respectively. In other words, our model forecasts the sea ice concentration for 4 weeks ahead using information from the preceding 12 weeks.

3.1 Decomposition

Firstly, based on the results of an explanatory data analysis, we decompose the input image into two components: trend and residual. Time series decomposition has enhanced forecasters efficiently Salles et al. (2019). In our image data, the trend component of \mathbf{X}_t , denoted as \mathbf{T}_t , is easily extracted through the utilization of a moving average filter (MA_K) with a size of K , an odd number less than L , as follows:

$$\mathbf{T}_t = MA_K(tpad(\mathbf{X}_t)),$$

where $\mathbf{T}_t(l, i, j) = \frac{1}{K} \sum_{k=-\lfloor K/2 \rfloor}^{\lfloor K/2 \rfloor} tpad(\mathbf{X}_t)(l + k, i, j)$, and $tpad(\cdot)$ represents a padding technique to preserve the time length, while $\mathbf{M}(l, i, j)$ denotes the (i, j) pixel value of the l -th image in \mathbf{M} .

The residual component, \mathbf{R}_t , is calculated by detrending the original input \mathbf{X}_t as follows: $\mathbf{R}_t = \mathbf{X}_t - \mathbf{T}_t$. Then, the components, \mathbf{T}_t and \mathbf{R}_t , are each utilized as input in their own U-Net architecture, as described in Figure 5. In other words, we employ two separate U-Nets for each component to forecast in a parallel fashion. From now on, since the process for the residual component is identical, we will only explain the process for the trend component.

3.2 Encoder

Our proposed method is designed to integrate multiple pieces of information from various datasets. At

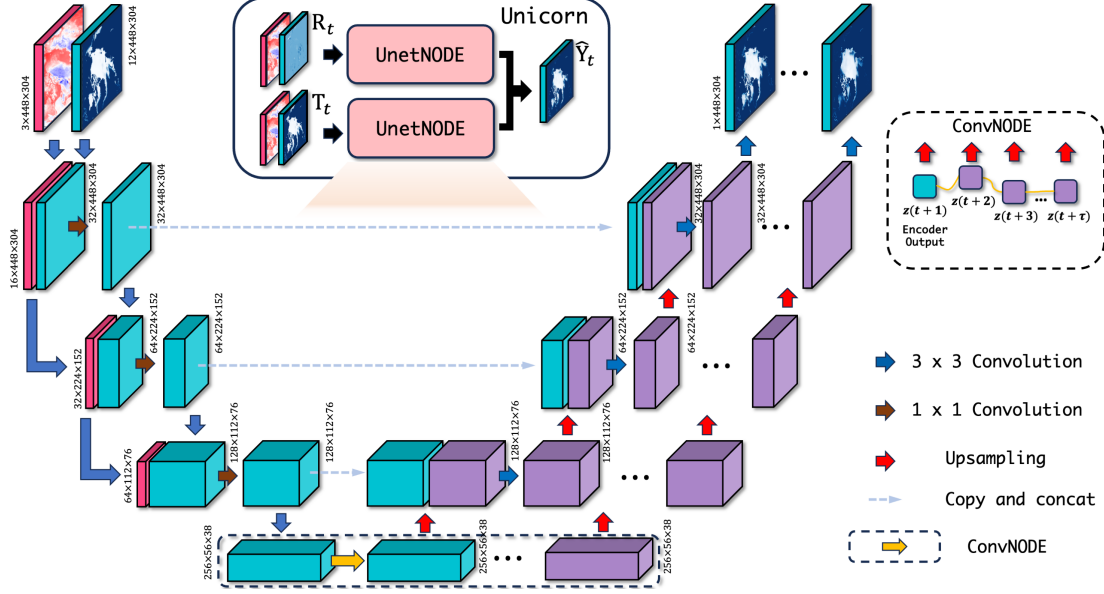


Figure 5: Overall architecture of our proposed model, Unicorn, in the middle above, and UnetNODE (example for trend component \mathbf{T}_t). Teal and red-colored boxes represent intermediate outputs of the encoder, while violet-colored boxes represent intermediate outputs of ConvNODE and decoder.

the time point t , the encoder takes three images: the component of the SIC (\mathbf{T}_t or \mathbf{R}_t), the TB (\mathbf{B}_t), and the SIA (\mathbf{S}_t). Because the channels of SIC and ancillary images have different semantics (time points in SIC and dimensions of variables in ancillary images), the contracting path of the encoder is split into two paths: the main path and the ancillary path. The main path takes the components of the SIC, and its architecture follows the typical type of the U-Net encoder. The main path comprises recursively stacked blocks combined by 3×3 convolutions, batch normalization, ReLU activation function, and 2×2 max pooling. The ancillary path takes the concatenated ancillary images, $[\mathbf{B}_t; \mathbf{S}_t] \in \mathbb{R}^{3 \times (H \times W)}$ and consists of the same blocks as the main path. The output of the main path is integrated with that from the auxiliary path using a 1×1 convolution. Consequently, the encoder seamlessly fuses multiple images, and the recursive fusions via 1×1 convolutions provide additional information to the up-sampling process by concatenating copied features. Let the output of the encoder be $\mathbf{z}_t(0)$ at time point t , then the process in the encoder can be written as follows:

$$\begin{aligned} \mathbf{A}_t^{(1)} &= \text{Convblock}^{(1)}(\text{cat}(\mathbf{B}_t, \mathbf{S}_t)) \\ \mathbf{T}_t^{(1)} &= \text{Convblock}^{(2)}(\mathbf{T}_t) \\ \mathbf{F}_t^{(1)} &= \text{Conv}_{1 \times 1}^{(1)}(\text{cat}(\mathbf{A}_t^{(1)}, \mathbf{T}_t^{(1)})) \end{aligned}$$

$$\begin{aligned} \mathbf{A}_t^{(2)} &= \text{Convblock}^{(3)}(\mathbf{A}_t^{(1)}) \\ \mathbf{F}_t^{(2)} &= \text{Conv}_{1 \times 1}^{(2)}(\text{cat}(\text{Convblock}^{(4)}(\mathbf{F}_t^{(1)}), \mathbf{A}_t^{(2)})) \\ \mathbf{A}_t^{(3)} &= \text{Convblock}^{(5)}(\mathbf{A}_t^{(2)}) \\ \mathbf{F}_t^{(3)} &= \text{Conv}_{1 \times 1}^{(3)}(\text{cat}(\text{Convblock}^{(6)}(\mathbf{F}_t^{(2)}), \mathbf{A}_t^{(3)})) \\ \mathbf{z}_t(0) &= \text{Convblock}^{(7)}(\mathbf{F}_t^{(3)}), \end{aligned}$$

where $\text{Conv}_{i \times i}$ is the convolutional layer with an $i \times i$ kernel, and Convblock is a block composed of two $[\text{Conv}_{3 \times 3}$, batch normalization, relu] operations. Additionally, cat is a concatenation operator along the time dimension.

3.3 ConvNODE

ConvNODE effectively captures the intricate spatiotemporal dynamics in sea ice images extracted through the encoder. It predicts the temporal evolution of the latent variable $\mathbf{z}_t(\kappa)$, derived from each component \mathbf{T}_t and \mathbf{R}_t , at the output image's timestamps using NODE framework, where the rate of change function is represented by the convolutional operation.

The theoretical foundation enabling this structure is as follows. By representing ODE as differential equations dependent on time k and solving them, we can derive changes in the variable over time. Let κ be the current time point and $\kappa + 1$ be the next time point. The rate of change function for $\mathbf{z}_t(\kappa)$ is denoted by

$f(\mathbf{z}_t(k))$. Based on these definitions, the temporal evolution of $\mathbf{z}_t(\kappa)$ can be calculated using ODE as follows:

$$\mathbf{z}_t(\kappa + 1) = \mathbf{z}_t(\kappa) + \int_{\kappa}^{\kappa+1} f(\mathbf{z}_t(s))ds. \quad (1)$$

By defining Equation (1), we establish a strong foundation for predicting the intricate dynamics of latent variables. The effectiveness of applying the NODE framework relies on selecting the appropriate rate of change function, f , for a given purpose. Based on this understanding, Lim et al. (2023) defines the function f as a linear function, such as $f(\mathbf{z}_t(s)) = \mathbf{W}\mathbf{z}_t(s) + \mathbf{b}$, for time series forecasting of tabular datasets. To proficiently model the temporal dynamics of image sequences, we employ convolutional operations instead of a linear f . It is recognized for its ability to adeptly encapsulate both spatial and temporal information within image and video datasets Simonyan and Zisserman (2014). Aligned with the ODE approach, the temporal dynamics of $\mathbf{z}_t(\kappa)$ as a function over time are defined as follows:

$$\mathbf{z}_t(\kappa + 1) = \mathbf{z}_t(\kappa) + \int_{\kappa}^{\kappa+1} Conv_{3 \times 3}(\mathbf{z}_t(k))dk. \quad (2)$$

Through ConvNODE in Equation (2), the latent variables are computed and passed to the decoder as inputs. This structure effectively combines the advantages of NODE and convolutional operations. Therefore, it accurately reflects spatiotemporal variations in latent variables extracted from sea ice and ancillary images.

3.4 Decoder

The decoder utilizes the outputs, $\mathbf{z}_t(0), \dots, \mathbf{z}_t(\tau-1)$, to forecast the future SIC from $(t+1)$ to $(t+\tau)$ time points, denoted as \mathbf{Y}_t . Contrary to the encoder, which has only two paths (main and ancillary paths), the decoder consists of τ expansive paths to predict τ SIC by leveraging the corresponding latent variable $\mathbf{z}_t(\kappa), \kappa = 0, \dots, \tau-1$. Contextual information within $\mathbf{z}_t(\kappa)$ is expanded by 2×2 upsampling convolutions in each expansive path. Subsequently, it is combined with the output of the encoder through the enhanced skip connection (copy and concatenating) with ancillary information. After three upsampling processes, the output image has the same size as the original input, as

follows :

For $\kappa = 0, \dots, \tau-1$,

$$\begin{aligned} \mathbf{z}_t^{(1)}(\kappa) &= Convblock_{\kappa}^{(8)}(cat(upsample_{\kappa}^{(1)}(\mathbf{z}_t(\kappa)), \mathbf{F}_t^{(3)})) \\ \mathbf{z}_t^{(2)}(\kappa) &= Convblock_{\kappa}^{(9)}(cat(upsample_{\kappa}^{(2)}(\mathbf{z}_t^{(1)}(\kappa)), \mathbf{F}_t^{(2)})) \\ \mathbf{z}_t^{(3)}(\kappa) &= Convblock_{\kappa}^{(10)}(cat(upsample_{\kappa}^{(3)}(\mathbf{z}_t^{(2)}(\kappa)), \mathbf{F}_t^{(1)})) \\ \tilde{\mathbf{T}}_t &= Conv_{3 \times 3}^{(1)}(cat(\mathbf{z}_t^{(3)}(0), \dots, \mathbf{z}_t^{(3)}(\tau-1))), \end{aligned}$$

where *upsample* is an operation to increase the spatial resolution of the input, performed using transposed convolution. $\sigma(\cdot)$ denotes the sigmoid activation function for scaling outputs.

Simultaneously applying the entire process from the encoder to the decoder with \mathbf{R}_t , we obtain $\tilde{\mathbf{R}}_t$, and subsequently, the predictions are calculated as $\hat{\mathbf{Y}}_t = \sigma(\tilde{\mathbf{T}}_t + \tilde{\mathbf{R}}_t)$.

3.5 Training

This section introduces a training process for our proposed model. Many existing approaches, such as Ali and Wang (2022); Ren and Li (2023), utilized the MSE as a loss function for the prediction tasks. Because the SIC takes values in $[0, 1]$ like a normalized pixel intensity, the binary cross-entropy (BCE) can be used for a dissimilarity criterion between two images Creswell et al. (2017). Moreover, de León et al. (2022) demonstrated that models minimizing the BCE tend to outperform others that minimize different loss functions, such as a mean squared error (MSE), particularly in tasks related to image reconstruction. Given the target \mathbf{Y}_t and output $\hat{\mathbf{Y}}_t$, our model is instructed to minimize the BCE loss \mathcal{L} as follows:

$$\begin{aligned} \mathcal{L}(\Theta; \mathcal{T}) &= \sum_{t \in \mathcal{T}} \sum_{l=1}^{\tau} \sum_{i,j} \mathbf{Y}_t(l, i, j) \log \hat{\mathbf{Y}}_t(l, i, j; \Theta) + \\ &\quad (1 - \mathbf{Y}_t(l, i, j)) \log(1 - \hat{\mathbf{Y}}_t(l, i, j; \Theta)), \end{aligned}$$

where Θ is the entire parameters of the model, \mathcal{T} is a time point set of the training dataset, and $\mathbf{Y}_t(l, i, j)$ and $\hat{\mathbf{Y}}_t(l, i, j)$ denote (i, j) element of target and predicted image for $(t+l)$ time point, respectively. The model parameters Θ can be updated by stochastic gradient descent-based algorithms.

4 Experiment

This section introduces our evaluation procedure and metrics used in our experiment and presents performance comparisons between the proposed model

and existing ones. To ensure reliable results, we implemented a cross-validation strategy using our dataset of SIC, TB, and SIA images from 1998 to 2021. The data are divided into four overlapping fifteen-year periods, and each new period begins three years after the previous one. In each segment, the first 11 years are designated for training, the 12th year for validation, and the last three years for testing. This sliding window approach allows for comprehensive coverage and utilization of the dataset over time.

For training and validation, batch sizes are set to 8, while a batch size of 1 was used for the test set to facilitate detailed performance analysis. The AdamW optimizer Loshchilov and Hutter (2017) with a learning rate of 0.001 is used and an early stopping mechanism is applied if no improvement in validation loss is observed for 50 iterations. All implementations, including benchmarks, were conducted using PyTorch on an A10 GPU and CentOS Linux. The source code is publicly accessible at <https://anonymous.4open.science/r/unicorn-461B>.

4.1 Metrics

This study assesses sea ice forecasting models through two tasks: SIC and SIE forecasting. For SIC forecasting, mean absolute error (MAE) and root mean squared error (RMSE) are selected as evaluation metrics. These metrics are widely used for assessing the accuracy of predicted sea ice concentrations at individual pixels in the forecasted images. All metrics are computed using pixel values within non-land ice areas to ensure a precise evaluation specifically targeting sea ice. We denote \mathcal{N} as the set of pixel coordinates representing non-land ice areas in the images. Thus, MAE and RMSE between the ground truth (\mathbf{Y}) and predicted value ($\hat{\mathbf{Y}}$) are computed as follows:

$$\text{MAE} = \frac{1}{\tau N |\mathcal{T}'|} \sum_{t \in \mathcal{T}'} \sum_{l=1}^{\tau} \sum_{(i,j) \in \mathcal{N}} \left\| \mathbf{Y}_t(l, i, j) - \hat{\mathbf{Y}}_t(l, i, j) \right\|_1$$

$$\text{RMSE} = \sqrt{\frac{1}{\tau N |\mathcal{T}'|} \sum_{t \in \mathcal{T}'} \sum_{l=1}^{\tau} \sum_{(i,j) \in \mathcal{N}} \left\| \mathbf{Y}_t(l, i, j) - \hat{\mathbf{Y}}_t(l, i, j) \right\|_2^2},$$

where \mathcal{T}' represents the time point set of the test dataset, and N denotes the cardinality of \mathcal{N} , i.e., $|\mathcal{N}|$.

For SIE forecasting, considering the critical importance of accurately predicting sea ice areas, we utilize the integrated ice-edge error (IIEE) metric. We also employ the F1-score, accuracy, and mean intersection over union (mIoU), which are widely used in computer vision tasks. To evaluate SIE forecasting performance,

both ground truth and predicted SIC images are transformed into binary images using a threshold of 0.15. Let \mathbf{Y}_t and $\hat{\mathbf{Y}}_t$ represent the transformed images from \mathbf{Y}_t and $\hat{\mathbf{Y}}_t$, respectively, where $\mathbf{Y}_t, \hat{\mathbf{Y}}_t \in \{0, 1\}^{\tau \times (H \times W)}$. The metrics for SIE forecasting are computed as follows:

$$\text{IIEE} = \frac{1}{\tau |\mathcal{T}'|} \sum_{t \in \mathcal{T}'} \sum_{l=1}^{\tau} \sum_{(i,j) \in \mathcal{N}} \left\| \mathbf{Y}_t(l, i, j) - \hat{\mathbf{Y}}_t(l, i, j) \right\|_1$$

$$\text{IoU}_t = \frac{1}{\tau} \sum_{l=1}^{\tau} \frac{|\{(i, j) | \mathbf{Y}_t(l, i, j) = 1\} \cap \{(i, j) | \hat{\mathbf{Y}}_t(l, i, j) = 1\}|}{|\{(i, j) | \mathbf{Y}_t(l, i, j) = 1\} \cup \{(i, j) | \hat{\mathbf{Y}}_t(l, i, j) = 1\}|}$$

$$\text{mIoU} = \frac{1}{|\mathcal{T}'|} \sum_{t \in \mathcal{T}'} \text{IoU}_t, \quad \text{F1} = \frac{2 \cdot \text{TP}}{2 \cdot \text{TP} + \text{FP} + \text{FN}},$$

where TP, FP, and FN denote the number of true positives, false positives, and false negatives, respectively.

4.2 Compared Models

For comparative analysis, we evaluate seven benchmark models, including domain-specific ones, alongside our proposed model. Each baseline model retains the structure and hyperparameter configurations of its original version, with adjustments to facilitate the generation of τ prediction images from L input images. Additionally, we applied zero padding to convolutional operations wherever necessary to maintain the size of the images. The list of benchmark models and their summaries are as follows:

1. CNN Kim et al. (2021): the standard neural network for image data.
2. ConvLSTM Kim et al. (2021): A neural network architecture that combines CNN and LSTM, suitable for spatiotemporal forecasting.
3. U-Net Ronneberger et al. (2015): the foundational model for image segmentation, with numerous variants proposed for sea ice forecasting applications.
4. DU-Net: a U-Net-based sea ice forecaster with a decomposition method for DLinear in Zeng et al. (2022).
5. NU-Net: a U-Net-based sea ice forecaster with a decomposition method for NLinear in Zeng et al. (2022).
6. SICNet (CBAM) Ren et al. (2022): the U-Net-based domain-specific model for sea ice forecasting with channel and spatial attention.

Table 1: Experimental results of forecasting models. The most favorable value is highlighted in bold.

Task	SIC		SIE		
	MAE ↓	RMSE ↓	IIEE ↓	mIoU ↑	F1 ↑
CNN	0.031	0.096	1975.711	0.879	0.935
ConvLSTM	0.035	0.096	2124.798	0.873	0.932
U-Net	0.024	0.077	1428.064	0.911	0.953
DU-Net	0.025	0.075	1409.271	0.912	0.953
NU-Net	0.024	0.076	1401.810	0.912	0.954
SICNet (CBAM)	0.024	0.074	1374.186	0.915	0.955
SICNet (TSAM)	0.024	0.075	1402.616	0.912	0.954
Unicorn	0.023	0.071	1270.477	0.920	0.958

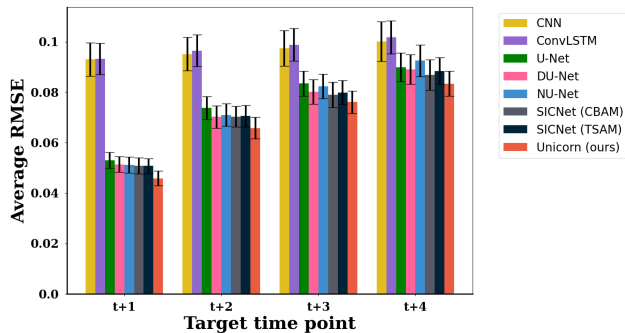


Figure 6: Average RMSE with its interval, average ± 1 standard deviation, of forecasting models across different target time points.

- SICNet (TSAM) Ren et al. (2022): the U-Net-based domain-specific model for sea ice forecasting, where temporal attention replaces channel attention.

4.3 SIC forecasting performance

For the SIC forecasting task, we assess both benchmarks and Unicorn using two metrics, MAE and RMSE, as defined in Section 4.1. Performance results on the test dataset are presented in Table 1, demonstrating that Unicorn outperforms other models in both metrics. Specifically, Unicorn exhibits significant superiority over all benchmarks in the MAE metric, which is known for its robustness against outliers, achieving an average improvement of 12.11% (with an improvement of 4.17% in comparison to the next best model). In evaluation using the RMSE, Unicorn achieved an average 11.60% improvement versus other models with an improvement of 4.05% compared to SICNet (CBAM).

Figure 6 displays average MAE and RMSE across different target time points. Unicorn has the lowest average errors at each target time point. Figure 7 displays the 4-week ahead SIC forecasting results of selected

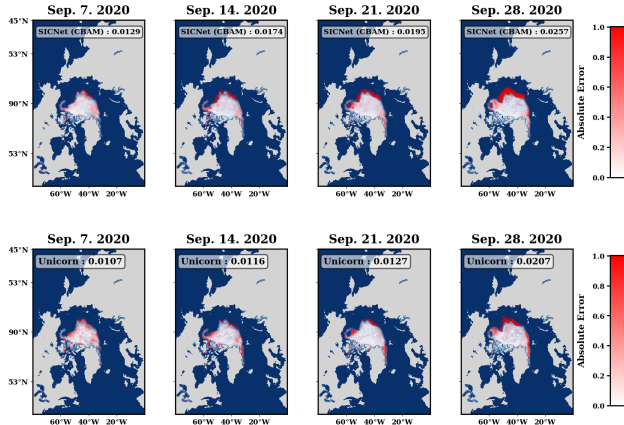


Figure 7: SIC forecasting results. From the top row to the bottom row, the images showcase the results from SICNet (CBAM), and Unicorn, along with their MAE values. The red color represents the absolute error between prediction and ground truth.

models: CNN, U-Net, SICNet (CBAM), and Unicorn. The red color represents the absolute error between prediction and ground truth. At the top of the images, the MAE value is presented alongside the model’s name. Unicorn can capture a increasing trend in the edge region of the sea ice, whereas the other models fail to do so as the target time point increases.

4.4 SIE forecasting performance

In the sea ice domain, accurate SIE forecasting is equally as important as SIC forecasting. Table 1 presents the performance of SIE forecasting with three metrics: IIEE, mIoU, and F1-score. In all three metrics, Unicorn outperforms the state-of-the-art models. The Unicorn model exhibits enhancements in SIE forecasting, particularly in the IIEE metric, where it shows an average improvement of 17.59% with a 7.55% improvement over its closest competitor, SICNet (CBAM). The mIoU and F1 scores still signify advancements over existing models. These improvements underscore Unicorn’s consistent accuracy and reliability across varying ice conditions.

Figure 8 shows the average IIEE and mIoU for different target time points, and Unicorn has the lowest IIEE and highest mIoU for each target time point compared to other models. Figure 9 displays the 4-week ahead SIE forecasting results of SICNet (CBAM), the next best model, and Unicorn. The first row of Figure 9 presents the results from June 7, 2020, to July 27, 2020, during a period when the sea ice exhibits a decreasing pattern as shown in Figure 7. The second row

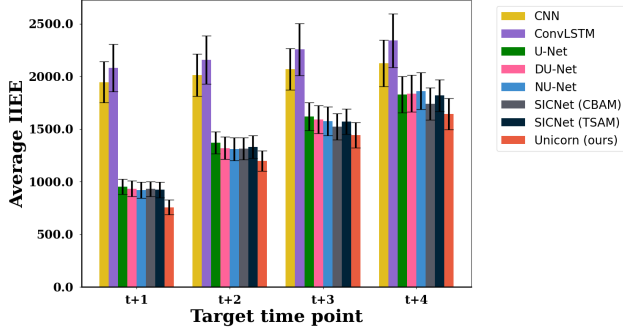


Figure 8: Average IIEE with its interval, average ± 1 standard deviation, of forecasting models across different target time points.

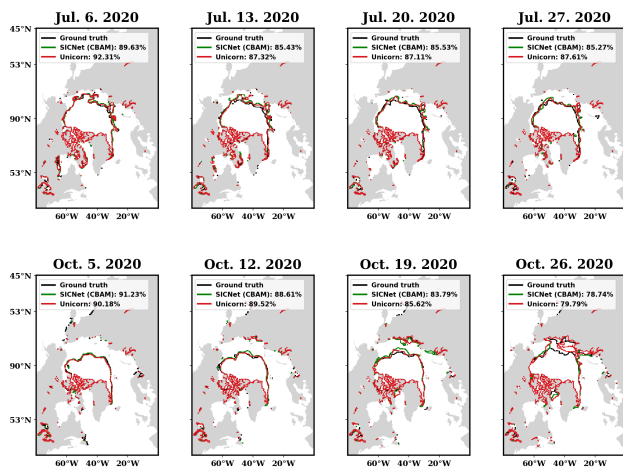


Figure 9: SIE forecasting results. In the image, the boundaries of SIE forecasting for SICNet (CBAM), Unicorn, and the ground truth are shown along with their mIoU values.

of Figure 9 presents the results from October 5, 2020, to October 26, 2020, during a period when the sea ice exhibits an increasing pattern. The black line represents the ground truth sea ice edge, while the green and red lines represent the sea ice edge based on SICNet (CBAM) and Unicorn results, respectively. At the top of the images, the mIoU values between the ground truth and prediction model are displayed alongside the model’s name. In both cases (decreasing and increasing periods), Unicorn outperforms SICNet (CBAM).

4.5 Ablation study

In this study, we conducted an ablation analysis within the Unicorn model to evaluate the impact of different components – DCMP, ConvNODE, and ancillary datasets – on predictions of SIC and SIE. This

Table 2: Experimental results of the ablation study. The most favorable value is highlighted in bold.

task	SIC		SIE		
	MAE ↓	RMSE ↓	IIEE ↓	mIoU ↑	F1 ↑
U-Net	0.0245	0.0776	1428.0643	0.9107	0.9528
Unicorn w/o DCMP	0.0231	0.0713	1299.8065	0.9189	0.9574
Unicorn w/o ConvNODE	0.0231	0.0726	1302.4603	0.9181	0.9570
Unicorn w/o ancillary data	0.0238	0.0733	1376.9587	0.9141	0.9547
Unicorn	0.0228	0.0707	1270.4770	0.9204	0.9583

methodical removal helps to isolate and assess the individual contributions of these components, which are summarized in Table 2. By structuring the analysis, we aim to clarify each component’s unique role in enhancing model performance.

Our findings show that removing the DCMP block leads to a reduction in IIEE for SIE predictions by about 2.26%, emphasizing its role in managing time-series complexities. The omission of ConvNODE, on the other hand, resulted in significant accuracy losses, with increases in MAE by 1.30% and RMSE by 2.62% for SIC predictions. This illustrates how vital ConvNODE is in maintaining high precision in forecasting. The removal of ancillary data caused the most substantial impact, leading to notable deterioration in both SIC and SIE predictions—MAE increased by 4.20%, RMSE by 3.55%, IIEE by 7.73%, mIoU by 0.69%, and F1 score by 0.38%. These results, validated through rigorous cross-validation, highlight each component’s essential role in sustaining the model’s effectiveness across diverse conditions.

The comprehensive evaluation through sliding window analysis confirms that Unicorn achieves optimal performance when fully integrated. Even when components are removed, it significantly outperforms the baseline model, U-Net. This ablation study serves to validate the effectiveness of our proposed components. Furthermore, we delve into investigating the effects of DCMP in the Appendix.

5 Conclusion

Our study presents a novel approach to sea ice forecasting from two perspectives. Firstly, we developed an enhanced ConvNODE model through local time series decomposition to account for the non-stationarity of sea ice dynamics. Secondly, we propose integrating additional information from brightness temperature and sea ice age. Through real data analysis from 1998 to 2021, Unicorn shows improvements, with a 12% enhancement in the average MAE for SIC and approximately an 18% improvement in the primary SIE metric IIEE. This advancement is expected to greatly enhance

the precision of sea ice forecasts and stimulate further research in climate and related fields.

Although the proposed model achieves high-quality performance, it still has some limitations. One notable limitation is its high computing cost. Our model generates latent variables and images in multiple timesteps through respective upsampling paths, resulting in a relatively higher number of trainable parameters than other models. Another limitation is the absence of explainability. Due to the nature of neural networks, the outputs of the proposed model are challenging to explain. We propose incorporating our model with an interpretable neural network module such as the variable selection network Lim et al. (2021) as a potential solution. Another approach is to define the sea ice forecasting problem as a multi-task problem, encompassing both SIC and SIE forecasting, as demonstrated in prior work Ali and Wang (2022). In this setup, canonical correlation analysis can be employed to extract canonical information from multiple tasks Rakowski and Lippert (2023), aiding in learning shared and task-specific representations and providing explanations for forecasting results. We consider addressing these issues as part of our future work.

References

- Ali, S. and Wang, J. (2022). Mt-icenet - a spatial and multi-temporal deep learning model for arctic sea ice forecasting. In *2022 IEEE/ACM International Conference on Big Data Computing, Applications and Technologies (BDCAT)*, pages 1–10. IEEE.
- Andersson, T. R., Hosking, J. S., Pérez-Ortiz, M., Paige, B., Elliott, A., Russell, C., Law, S., Jones, D. C., Wilkinson, J., Phillips, T., et al. (2021). Seasonal arctic sea ice forecasting with probabilistic deep learning. *Nature communications*, 12(1):5124.
- Chen, R. T., Rubanova, Y., Bettencourt, J., and Duvenaud, D. (2018). Neural ordinary differential equations. In *Proceedings of the 32nd International Conference on Neural Information Processing Systems*, pages 6572–6583.
- Chen, X., Valencia, R., Soleymani, A., Scott, K. A., Xu, L., and Clausi, D. A. (2023). Calibration of uncertainty in sea ice concentration retrieval with an auxiliary prediction interval estimator. *IEEE Geoscience and Remote Sensing Letters*, 20:1–5.
- Chi, J. and Kim, H. (2017). Prediction of arctic sea ice concentration using a fully data driven deep neural network. *Remote. Sens.*, 9:1305.
- Choi, M., Silva, L. W. A. D., and Yamaguchi, H. (2019). Artificial neural network for the short-term prediction of arctic sea ice concentration. *Remote. Sens.*, 11:1071.
- Choi, S. (2020). Utilizing unet for the future traffic map prediction task traffic4cast challenge 2020. *arXiv preprint arXiv:2012.00125*.
- Collow, T. W., Wang, W., Kumar, A., and Zhang, J. (2015). Improving arctic sea ice prediction using piomas initial sea ice thickness in a coupled ocean–atmosphere model. *Monthly Weather Review*, 143(11):4618–4630.
- Creswell, A., Arulkumaran, K., and Bharath, A. A. (2017). On denoising autoencoders trained to minimise binary cross-entropy. *arXiv preprint arXiv:1708.08487*.
- de León, G., Cesbron, J., Klein, P., Leandri, P., and Losa, M. (2022). Novel methodology to recover road surface height maps from illuminated scene through convolutional neural networks. *Sensors*, 22(17):6603.
- Fernández, J. G. and Mehrkanoon, S. (2021). Broad-unet: Multi-scale feature learning for nowcasting tasks. *Neural Networks*, 144:419–427.
- He, J., Zhao, Y., Yang, D., Zhu, K., and Deng, X. (2022). An improved convlstm network for arctic sea ice concentration prediction. In *OCEANS 2022, Hampton Roads*, pages 1–5. IEEE.
- Huang, X., Zhang, B., Feng, S., Ye, Y., and Li, X. (2023). Interpretable local flow attention for multi-step traffic flow prediction. *Neural networks*, 161:25–38.
- Kim, E., Kruse, P., Lama, S., Bourne, J., Hu, M., Ali, S., Huang, Y., and Wang, J. (2021). Multi-task deep learning based spatiotemporal arctic sea ice forecasting. In *2021 IEEE International Conference on Big Data (Big Data)*, pages 1847–1857. IEEE.
- Kim, M., Lee, J., Choi, L., and Choi, M. (2023). Polarlan: Creating realistic arctic sea ice concentration images with user-defined geometric preferences. *Engineering Applications of Artificial Intelligence*, 126:106920.
- Kim, S., Park, S., Chung, S., Lee, J., Lee, Y., Kim, H., Prabhat, M., and Choo, J. (2019). Learning to focus and track extreme climate events. In *30th British Machine Vision Conference, BMVC 2019, Cardiff, UK, September 9-12, 2019*, page 11. BMVA Press.

- Kraemer, S. A., Ramachandran, A., Onana, V. E., Li, W. K. W., and Walsh, D. A. (2024). A multiyear time series (2004–2012) of bacterial and archaeal community dynamics in a changing arctic ocean. *ISME Communications*, 4.
- Kwok, R. (2018). Arctic sea ice thickness, volume, and multiyear ice coverage: losses and coupled variability (1958–2018). *Environmental Research Letters*, 13.
- Li, D., Tang, P., Zhang, R., Sun, C., Li, Y., Qian, J., Liang, Y., Yang, J., and Zhang, L. (2021). Robust blood cell image segmentation method based on neural ordinary differential equations. *Computational and Mathematical Methods in Medicine*, 2021.
- Li, W. K. W., McLaughlin, F. A., Lovejoy, C., and Carmack, E. C. (2009). Smallest algae thrive as the arctic ocean freshens. *Science*, 326:539 – 539.
- Lim, B., Arık, S. Ö., Loeff, N., and Pfister, T. (2021). Temporal fusion transformers for interpretable multi-horizon time series forecasting. *International Journal of Forecasting*, 37(4):1748–1764.
- Lim, S., Park, J., Kim, S., Wi, H., Lim, H., Jeon, J., Choi, J., and Park, N. (2023). Long-term time series forecasting based on decomposition and neural ordinary differential equations. In *2023 IEEE International Conference on Big Data (BigData)*, pages 748–757. IEEE.
- Liu, Q., Zhang, R., Wang, Y., Yan, H., and Hong, M. (2021). Daily prediction of the arctic sea ice concentration using reanalysis data based on a convolutional lstm network. *Journal of Marine Science and Engineering*, 9:330.
- Loshchilov, I. and Hutter, F. (2017). Decoupled weight decay regularization. In *International Conference on Learning Representations*.
- Meier, W. N., Stewart, J. S., Wilcox, H., Scott, D. J., and Hardman, M. A. (2022). DMSP SSM/I-SSMIS Daily Polar Gridded Brightness Temperatures, Version 6. <https://doi.org/10.5067/MXJL42WSXTS1>.
- Notz, D. and Stroeve, J. C. (2016). Observed arctic sea-ice loss directly follows anthropogenic co2 emission. *Science*, 354:747 – 750.
- Paoletti, M. E., Haut, J. M., Plaza, J., and Plaza, A. (2019). Neural ordinary differential equations for hyperspectral image classification. *IEEE Transactions on Geoscience and Remote Sensing*, 58(3):1718–1734.
- Pithan, F. and Mauritsen, T. (2014). Arctic amplification dominated by temperature feedbacks in contemporary climate models. *Nature Geoscience*, 7:181–184.
- Rakowski, A. and Lippert, C. (2023). Dcid: Deep canonical information decomposition. In *Joint European Conference on Machine Learning and Knowledge Discovery in Databases*, pages 20–35. Springer.
- Rantanen, M., Karpechko, A. Y., Lipponen, A., Nordling, K., Hyvärinen, O., Ruosteenoja, K., Vihma, T., and Laaksonen, A. (2022). The arctic has warmed nearly four times faster than the globe since 1979. *Communications Earth & Environment*, 3.
- Ren, Y. and Li, X. (2023). Predicting the daily sea ice concentration on a sub-seasonal scale of the pan-arctic during the melting season by a deep learning model. *IEEE Transactions on Geoscience and Remote Sensing*.
- Ren, Y., Li, X., and Zhang, W. (2022). A data-driven deep learning model for weekly sea ice concentration prediction of the pan-arctic during the melting season. *IEEE Transactions on Geoscience and Remote Sensing*, 60:1–19.
- Ronneberger, O., Fischer, P., and Brox, T. (2015). U-net: Convolutional networks for biomedical image segmentation. In *Medical Image Computing and Computer-Assisted Intervention–MICCAI 2015: 18th International Conference, Munich, Germany, October 5–9, 2015, Proceedings, Part III 18*, pages 234–241. Springer.
- Salles, R., Belloze, K., Porto, F., Gonzalez, P. H., and Ogasawara, E. (2019). Nonstationary time series transformation methods: An experimental review. *Knowledge-Based Systems*, 164:274–291.
- Screen, J. A. and Simmonds, I. (2010). The central role of diminishing sea ice in recent arctic temperature amplification. *Nature*, 464:1334–1337.
- Seo, M., Kim, D., Shin, S., Kim, E., Ahn, S., and Choi, Y. (2022). Simple baseline for weather forecasting using spatiotemporal context aggregation network. *arXiv preprint arXiv:2212.02952*.
- Shi, X., Chen, Z., Wang, H., Yeung, D.-Y., Wong, W.-K., and Woo, W.-c. (2015). Convolutional lstm network: A machine learning approach for precipitation nowcasting. *Advances in neural information processing systems*, 28.

- Simonyan, K. and Zisserman, A. (2014). Two-stream convolutional networks for action recognition in videos. *Advances in neural information processing systems*, 27.
- Song, W., Li, M., He, Q., Huang, D., Perra, C., and Liotta, A. (2018). A residual convolution neural network for sea ice classification with sentinel-1 sar imagery. *2018 IEEE International Conference on Data Mining Workshops (ICDMW)*, pages 795–802.
- Sumata, H., de Steur, L., Divine, D. V., Granskog, M. A., and Gerland, S. (2023). Regime shift in arctic ocean sea ice thickness. *Nature*, 615:443 – 449.
- Tschudi, M., Meier, W. N., Stewart, J. S., Fowler, C., and Maslanik, J. (2019). Ease-grid sea ice age, version 4.
- Wang, L., Yuan, X., Ting, M., and Li, C. (2016). Predicting summer arctic sea ice concentration intraseasonal variability using a vector autoregressive model. *Journal of Climate*, 29:1529–1543.
- Wang, W., Chen, M., and Kumar, A. (2013). Seasonal prediction of arctic sea ice extent from a coupled dynamical forecast system. *Monthly Weather Review*, 141:1375–1394.
- Wei, J., Hang, R., and Luo, J. (2022). Prediction of pan-arctic sea ice using attention-based lstm neural networks. In *Frontiers in Marine Science*.
- Wunderling, N., Willeit, M., Donges, J. F., and Winkelmann, R. (2020). Global warming due to loss of large ice masses and arctic summer sea ice. *Nature Communications*, 11.
- Yuan, X., Chen, D., Li, C., Wang, L., and Wang, W. (2016). Arctic sea ice seasonal prediction by a linear markov model. *Journal of Climate*, 29(22):8151–8173.
- Zeng, A., Chen, M.-H., Zhang, L., and Xu, Q. (2022). Are transformers effective for time series forecasting? In *AAAI Conference on Artificial Intelligence*.

Appendix

A1. Time series decomposition effects on distribution shift

As indicated in Figure 2, the sea ice data showed a clear trend, leading us to expect a significant enhancement in model performance with the introduction of the DCMP block. However, contrary to our expectations, as shown in Table 2 the DCMP block yielded unexpected outcomes, revealing that the DCMP block plays only a minor role.

To discern the cause, we normalized the mean of SIC and SIE data of the training and testing sets using the mean and standard deviation of the training set for comparison as follows:

$$\begin{aligned} \bar{Y}_t(l) &= \frac{1}{N} \sum_{(i,j) \in \mathcal{N}} Y_t(l, i, j) \\ \bar{Y}_{\mathcal{T}} &= \frac{1}{\tau|\mathcal{T}|} \sum_{t \in \mathcal{T}} \sum_{l=1}^{\tau} \bar{Y}_t(l) \\ s_{\mathcal{T}} &= \sqrt{\frac{\sum_{t \in \mathcal{T}} \sum_{l=1}^{\tau} (\bar{Y}_t(l) - \bar{Y}_{\mathcal{T}})^2}{\tau|\mathcal{T}| - 1}} \\ z_t(l) &= \frac{\bar{Y}_t(l) - \bar{Y}_{\mathcal{T}}}{s_{\mathcal{T}}}, \end{aligned}$$

where \mathcal{T} and \mathcal{T}' respectively represent the time points of the training and testing datasets, and N denotes the cardinality of NLIA, i.e. $|\mathcal{N}|$.

Despite the rapid decrease in sea ice Wei et al. (2022), our analysis of our dataset, as can be seen in Figure 10, revealed minimal differences in the distribution between the training and testing sets with equation (3). This observation led us to question the significant impact of the DCMP block, in accordance with the proposition put forth in Zeng et al. (2022).

Thus, we designed an additional experiment to rigorously assess the robustness of the DCMP block and its predictive accuracy using data with seasonal variation. We trained our model on data from October to March of one year, a period depicted in Figure 11, where the sea ice concentration and extent are either stable or increasing. The model was then tested on data from April to September to evaluate its ability to predict the declining trend of sea ice typically observed from July to September. Interestingly, unlike the overall data, Figure 10 demonstrates a significant difference in the distribution between the training and testing sets.

In this experiment, we followed the same experimental setup as described in Section 4, excluding the early stopping criteria due to the absence of a validation

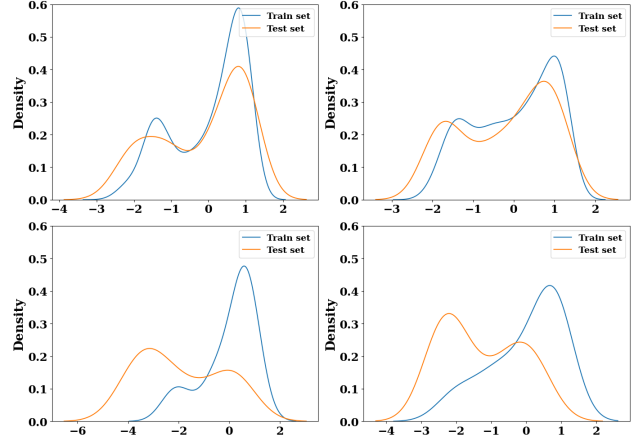


Figure 10: The top row shows the mean of SIC(left) and SIE(right) distribution of train and test sets from Jun. 1998 to Jun. 2021. The row below shows the mean of SIC (left) and SIE (right) distribution of train and test sets from Oct. 2019 to Sep. 2020.

Table 3: Experimental results of the supplementary test in SIC and SIE forecasting tasks. The lowest value is bolded.

Task	SIC		SIE		
	MAE	RMSE	IIEE	mIoU	F1
Unicorn w/o DCMP	0.097	0.223	8697.083	0.481	0.648
Unicorn	0.066	0.166	5210.241	0.615	0.759

set. The averaged results for July to September across 2018, 2019, and 2020 are presented in Table 3, highlighting the model’s performance on previously unseen data across different seasonal periods.

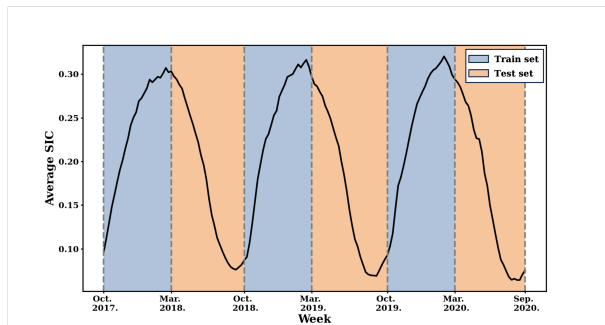


Figure 11: Mean Sea Ice Concentration (SIC) over six-month training (blue) and testing (orange) periods across three years, showcasing the seasonal dynamics of sea ice.